

Multidimensional images and aberrations in STEM

Eric R. Hoglund and Andrew R. Lupini

Citation: Chin. Phys. B, 2024, 33 (**9**): 096807. DOI: 10.1088/1674-1056/ad73b2
Journal homepage: http://cpb.iphy.ac.cn; http://iopscience.iop.org/cpb

What follows is a list of articles you may be interested in

Atomically self-healing of structural defects in monolayer WSe_2

Kangshu Li(李康舒), Junxian Li(李俊贤), Xiaocang Han(韩小藏), Wu Zhou(周武), and Xiaoxu Zhao(赵晓续)
Chin. Phys. B, 2024, 33 (**9**): 096804. DOI: 10.1088/1674-1056/ad641f

Symmetry quantification and segmentation in STEM imaging through Zernike moments

Jiadong Dan, Cheng Zhang, Xiaoxu Zhao(赵晓续), and N. Duane Loh
Chin. Phys. B, 2024, 33 (**8**): 086803. DOI: 10.1088/1674-1056/ad51f4

Controlled fabrication of freestanding monolayer SiC by electron irradiation

Yunli Da(笪蕴力), Ruichun Luo(罗瑞春), Bao Lei(雷宝), Wei Ji(季威), and Wu Zhou(周武)
Chin. Phys. B, 2024, 33 (**8**): 086802. DOI: 10.1088/1674-1056/ad6132

Selective linear etching of monolayer black phosphorus using electron beams

Yuhao Pan(潘宇浩), Bao Lei(雷宝), Jingsi Qiao(乔婧思), Zhixin Hu(胡智鑫), Wu Zhou(周武), Wei Ji(季威)
Chin. Phys. B, 2020, 29 (**8**): 086801. DOI: 10.1088/1674-1056/ab9438

Aberration-corrected scanning transmission electron microscopy for complex transition metal oxides

Qing-Hua Zhang(张庆华), Dong-Dong Xiao(肖东东), Lin Gu(谷林)
Chin. Phys. B, 2016, 25 (**6**): 066803. DOI: 10.1088/1674-1056/25/6/066803

SPECIAL TOPIC — Stephen J. Pennycook: A research life in atomic-resolution STEM and EELS

Multidimensional images and aberrations in STEM

Eric R. Hoglund[†] and Andrew R. Lupini[‡]

Center for Nanophase Materials Sciences, Oak Ridge National Laboratory, Oak Ridge, TN 37831, *United States*

(Received 7 June 2024; revised manuscript received 11 August 2024; accepted manuscript online 27 August 2024)

Recent advances in scanning transmission electron microscopy (STEM) have led to increased development of multi-dimensional STEM imaging modalities and novel image reconstruction methods. This interest arises because the main electron lens in a modern transmission electron microscope usually has a diffraction-space information limit that is significantly better than the real-space resolution of the same lens. This state-of-affairs is sometimes shared by other scattering methods in modern physics and contributes to a broader excitement surrounding multidimensional techniques that scan a probe while recording diffraction-space images, such as ptychography and scanning nano-beam diffraction. However, the contrasting resolution in the two spaces raises the question as to what is limiting their effective performance. Here, we examine this paradox by considering the effects of aberrations in both image and diffraction planes, and likewise separate the contributions of pre- and post-sample aberrations. This consideration provides insight into aberration-measurement techniques and might also indicate improvements for super-resolution techniques.

Keywords: scanning transmission electron microscopy (STEM), aberrations

PACS: 68.37.Ma, 07.78.+s, 68.37.Og, 87.64.Ee **DOI:** 10.1088/1674-1056/ad73b2

1. Introduction

It is a pleasure to write this paper on the occasion of Steve Pennycook's birthday. He was one of the pioneers of both high-resolution atomic number (Z) contrast scanning transmission electron microscopy (STEM) and then aberration correction. In addition to the researchers who designed the first aberration-correctors, one of the keys to making aberration-correction a practical tool was the work by established electron microscopists to realize the promise of this method. Of the established microscopists, Dr. Pennycook was one of the leaders in the development of the technique. In retrospect, the decision to adopt aberration-corrected imaging might seem obvious but, at the time, the conventional belief was that practical resolution improvement by this method might be impossible. Several factors were necessary, such as highly stable instruments, sophisticated computer control, rapid aberration measurement, and perhaps most importantly the vision of such scientists to pursue this dream.

It is also notable that Dr. Pennycook was one of the first to realize the importance of quantifying aberrations and STEM image signals. He led several works with some of the present authors and, in particular, was the first to achieve direct sub-Angstrom resolution in uncorrected STEM with Dr. Pete Nellist by carefully balancing aberrations.[1–3]

Peter Nellist, working closely with John Rodenburg, was also one of the key developers of ptychography in STEM, which is now the leading method to obtain the highest spatial resolution.[4] In order to recover the phase of the electron beam, ptychography uses a series of electron-optical Ronchigrams which are the main subject of the present paper. These images are named after Ronchi who pioneered the use of their optical equivalent in diagnosing light-optics.[5] In practice these images look a lot like bright field (BF) images, but they are not commonly used for direct imaging because they are strongly distorted by aberrations. However, this detriment provides a useful tool for aligning the microscope. In particular, the electron Ronchigram provides several methods for measuring and correcting aberrations in STEM. Recently, Ronchigrams have seen increasing use for 4D-STEM, where extensive processing can provide a reconstructed image in which the usual resolution limits do not apply.[6,7]

The general configuration for recording an electron Ronchigram is to have a coherent beam of electrons limited by a circular aperture and use lenses to form a converged probe at or near a sample, as shown in Fig. 1(a). The Ronchigram is formed by the transmitted beam at a detector in the far field. Scanning the probe across the sample and integrating the intensity of the transmitted beam on various detectors will give STEM images, with the characteristics of each image strongly depending on the properties of the detector. This arrangement contrasts to image formation in a conventional transmission electron microscope (CTEM) image, where a nearly parallel beam illuminates a sample and post-sample lenses are used to magnify a real-space image. In a STEM, the beam at the sample is strongly converging towards the sample and the detector is sitting in a diffraction plane. Even though the Ronchigram is formed in the diffraction plane the contrast will frequently resemble a CTEM or STEM bright-field image.

[†]Corresponding author. E-mail: hoglunder@ornl.gov
[‡]Corresponding author. E-mail: arl1000@ornl.gov

© 2024 Chinese Physical Society and IOP Publishing Ltd

Cowley and various coworkers pointed out that the magnification in the Ronchigram can be used to measure aberrations.[8–10] The question is how to determine the magnification? Cowley compared the BF image and the Ronchigram or looked at distinctive features such as circles of infinite magnification. Nion microscopes use calibrated shifts of the sample and analyze distortions within the Ronchigram.[11] Sawada and co-workers use the autocorrelation function of small patches.[12] Turning briefly to crystalline materials, Boothroyd showed that the Fourier transforms of crystalline Ronchigrams give 'comets' with a shape that depends on aberrations, which has been extended to provide fast measurement of aberrations in simple cases.[13,14] Ramasse has shown that contrast along particular directions can be used to measure high-order aberrations.[15] One promising avenue might be to train a neural network to rapidly analyze Ronchigrams. Resources like Ronchigram.com and abtem now provide a fast way to generate large sets of training data.

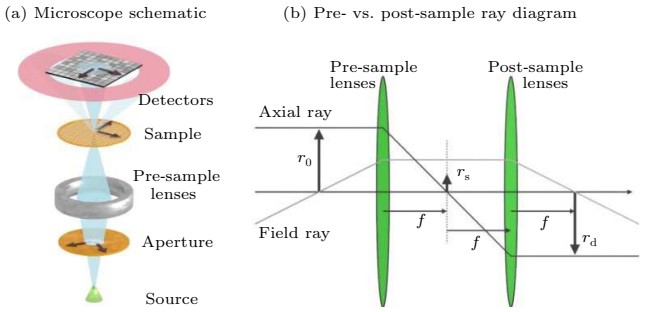


Fig. 1. (a) Cartoon illustration of 4D STEM. Electrons from the source are limited by an aperture and focused by a series of lenses to form a probe at the sample. Note that there are changes in magnification and rotation (not shown) between planes of interest. (b) Simplified illustration of an objective lens running in a symmetric mode with the lenses represented as pre- and post-sample fields. Focal lengths are given as f and the radius given as r at the entrance, sample, and diffraction planes. Axial and field rays are defined as seen from the sample.

Some of the present authors have also pointed out that a pixelated camera in the far-field can be considered as an array of STEM BF detectors at different angles.[16,17] Each pixel gives an image that will be shifted by a distance depending on the gradient of the aberration function. Measuring this shift provides a measurement of the aberrations, and digitally compensating for the shift allows a composite image to be constructed. This image can have a larger number of pixels than the number of probe positions,[17] delivering better spatial sampling and higher efficiency than a single monolithic detector.[18,19]

Through the principle of reciprocity, this arrangement is effectively equivalent to tilting the beam in TEM to give a Zemlin tableau.[20,21] A Zemlin tableau is probably the most well-established method to measure aberrations in BF CTEM, because the effective defocus and astigmatism[22] and the image shifts[21] depend on changes in the aberration function with angle.

One minor omission in most of the previous STEM work about Ronchigrams is that the post-sample aberrations from the projection, and possibly spectrometer, are usually ignored. The situation is similar in TEM, where it is typical to experimentally minimize and then neglect the pre-sample (probe) aberrations.

We note that ptychography involves finding a probe and an object function consistent with the acquired data through iterative methods, which implicitly provides a measurement of the aberrations. However, one might wonder what the effect of the projection system has on this process. For example, separating the instrumental function into a pre-sample (i.e., the true probe function) and post-sample function might lend to more accurate reconstructions. This leads to several questions: Why and when can we assume the post-sample spherical aberration does not significantly affect the resolution in diffraction modes? Although the convergence angle used to form a diffraction pattern is typically small, the scattering angles can be large. In this paper, we seek to examine the effect and magnitude of the effect of post-sample aberrations.

Reiterating this question, one might ask: Why is it that the resolution in an image is limited by aberrations, whereas the information in a diffraction pattern goes out to higher spatial frequencies? One potential answer lies in definitions: Resolution might be defined as purely a local property, separating two closely spaced objects, so it is perhaps an apples and oranges comparison. In the current work, we will mostly ignore this consideration and complications like dynamical scattering or diffraction, instead of taking a geometrical optics approach to this problem to find one part of the answer.

2. Types of aberrations

Aberrations are usually the main resolution limit in a modern TEM, which means that understanding and quantifying them is important. Here we will discuss a STEM but the discussion could be adapted to a TEM using the principle of reciprocity. As mentioned in the introduction, there are a variety of methods to measure aberrations.[23] The key stage in most of these methods is to think about where a particular ray intersects the sample (Fig. 1(b)).

2.1. Pre-sample

Consider a ray traveling parallel to the optic axis at some distance r from the axis, which is incident into a thin, ideal lens of focal length f as illustrated in Fig. 1(b). To simplify the discussion, we assume the small angle approximation, $\tan(\theta) = \sin(\theta) = \theta$, and that the ray is effectively coming from infinity. Initially, we have $r = r_0$ and $\theta_0 = 0$.

The deflection $\Delta\theta$ from a thin lens is

$$\Delta\theta = -\frac{r_0}{f} - \frac{\nabla\chi}{f}\left(\frac{r_0}{f}\right), \tag{1}$$

where χ is the aberration function and ∇ indicates the derivate. Propagating this same ray a distance f gives the position on the sample r_s as

$$r_s = \nabla\chi(\theta_s), \tag{2}$$

where the angle at the sample is approximately

$$\theta_s = -\frac{r_0}{f}. \tag{3}$$

In other words, the ray deviation is equal to the gradient of the aberration function, where we included defocus as an aberration. Because we took the incoming ray as coming from infinity, we essentially ignored source, gun, and condenser effects, which is usually reasonable for a microscope with a coherent source and aberration corrector.

2.2. Post-sample

The same ray leaves the sample at angle θ_s and, for a lens running in a symmetric mode, propagates a distance f to position $r_s + f\theta_s$ where the post-sample part of the objective lens gives another deflection. If we call the post-sample aberration function (ϕ), we have

$$\Delta\theta = -\frac{r_s + f\theta_s}{f} - \frac{\nabla\phi}{f}\left(\frac{r_s + f\theta_s}{f}\right). \tag{4}$$

Propagating this ray yet another distance f cancels the leading order dependence of position on r_s, corresponding to a diffraction plane, with the ray at

$$r_d = -f\theta_s - \nabla\chi_{post}\left(\theta_s + \frac{r_s}{f}\right) \approx -f\theta_s - \nabla\phi(\theta_s). \tag{5}$$

Again, to make the expressions simpler, we assume that the distance r_s is small, neglecting combination aberrations. It should then be clear that the r_d and r_s [Eqs. (2) and (5)] show similar dependence on their relevant aberration functions. The important difference is that the overall position in the diffraction pattern is dominated by $f\theta_s$.

The main point of this section is to show both the similarity and the difference between the effect of aberrations in the image and the diffraction planes. If the beam is close to the axis, as in a probe forming objective, then the probe-forming aberrations $\nabla\chi(\theta_s)$ are significant. However, at the post-sample diffraction plane, the deviation due to post-sample aberrations $\nabla\phi(\theta_s)$ is likely to be small compared to the position $f\theta_s$.

In other words, because the angular scale at the diffraction plane depends on the focal length, if pre- and post-sample aberrations are the same magnitude then the effect of post-sample aberration is far less significant in a diffraction plane than the pre-sample aberrations are in an image plane. For example, in a Ronchigram, the leading order ray deviation is $C_{10}\theta_s$, where C_{10} is of the order of nanometers, whereas f is of the order of millimeters, so explicitly separating this term from $\nabla\chi$ gives the ratio of absolute positions as

$$\frac{r_d}{r_s} = \frac{f\theta_s + \nabla\phi(\theta_s)}{C_{10}\theta_s + \nabla\chi(\theta_s)}. \tag{6}$$

Rather than consider the effect of other projector lenses, we point out that the chapter by Krivanek in the excellent *Handbook of Charged Particle Optics* shows that these can be mostly neglected when the beam is reasonably small and the focal length is long.

3. Measuring aberrations

A ray at angle θ_1 that is incident on a sample that is shifted by r_1 will arrive at a point R_1 deviated by aberrations, such that

$$R_1 = r_1 + \nabla\chi(\theta_1). \tag{7}$$

Repeating for a second ray,

$$R_2 = r_2 + \nabla\chi(\theta_2). \tag{8}$$

If we consider two Ronchigrams from two closely separated real-space probe positions (stage or probe shift, r_1 and r_2), the objects common to the two shadow images will appear at different angular positions (θ_1 and θ_2) in the Ronchigrams, allowing us to equate the rays R_1 and R_2, leading to

$$r_1 - r_2 = \nabla\chi(\theta_2) - \nabla\chi(\theta_1). \tag{9}$$

Or in other words, the gradient of the aberration function is tied to the image shifts. Notably, this result holds both for images acquired at different tilt angles and for Ronchigrams acquired at different probe positions. Consideration of the differential magnification in the Ronchigram can be used to tune the microscope.[11] Other methods including a contrast transfer function in the Ronchigram[24] or measuring the real-space shifts of images at different tilts might also be used.[16]

We temporarily define the local pre-sample angular magnification in the Ronchigram as the vector differential:

$$\mathrm{d}r_s = -\boldsymbol{C}\cdot\mathrm{d}\boldsymbol{\theta} \tag{10}$$

with $\boldsymbol{\theta} = (u, v)$. Or we might write this magnification as

$$\frac{\mathrm{d}\boldsymbol{\theta}}{\mathrm{d}r_s} = -\boldsymbol{C}^{-1}, \tag{11}$$

where we are using the matrix of second derivatives, evaluated at a particular angle:

$$\boldsymbol{C} = \begin{bmatrix} \frac{\partial^2\chi}{\partial u^2} & \frac{\partial^2\chi}{\partial u\partial v} \\ \frac{\partial^2\chi}{\partial v\partial u} & \frac{\partial^2\chi}{\partial v^2} \end{bmatrix}. \tag{12}$$

It is interesting to look at the first order terms in this expression, using the Krivanek aberration notation:

$$\boldsymbol{C} \approx \begin{bmatrix} C_{10} + C_{12a} + \cdots & C_{12b} + \cdots \\ C_{12b} + \cdots & C_{10} - C_{12a} + \cdots \end{bmatrix}. \tag{13}$$

We can see how this notation ties the local magnification to the derivatives of the aberration function at that angle. The important point is that the inverse of the magnification in a Ronchigram gives a measurement of the aberrations.[8,11,12] Notably, this inference assumes that we are accurately imaging angular space onto the detector. We also neglect the rotation due to round magnetic lenses, which can be added as rotation matrices.

We are now able to include post-sample aberrations. From the derivative of Eq. (5) in the previous section, we can write the differential post-sample magnification as

$$\frac{\mathrm{d}r_\mathrm{d}}{\mathrm{d}\theta} = -(f + \boldsymbol{D}), \tag{14}$$

where $\boldsymbol{D}$ like $\boldsymbol{C}$ is the derivative as in Eq. (12). Combining the expressions for $\mathrm{d}r_\mathrm{d}$ and $\mathrm{d}r_\mathrm{s}$ [Eqs. (11) and (14)] to eliminate $\mathrm{d}\theta$ gives the spatial magnification as

$$M = \frac{\mathrm{d}r_\mathrm{d}}{\mathrm{d}r_\mathrm{s}} = (f + \boldsymbol{D})\,\boldsymbol{C}^{-1}. \tag{15}$$

This expression combines both pre- and post-sample aberrations. Unfortunately, it is difficult to separate the pre- and post-sample aberrations in this expression because they are tied together in an awkward way.

We can seek an expression for the case where the matrix $\boldsymbol{C}$ is dominated by defocus, using a Neumann series to approximate the matrix inverse and retaining only the leading terms to give

$$\mathrm{d}r_\mathrm{d}\left(\boldsymbol{C} - \frac{C_{10}}{f}\boldsymbol{D}\right) \approx f\,\mathrm{d}r_\mathrm{s}. \tag{16}$$

We are assuming that the other aberrations are small compared to focus, so this might not be a good approximation where that condition is not met. The interesting point is that this equation shows that post-sample aberrations affect the Ronchigram magnification in a rather similar way to the pre-sample aberrations. The difference is the scaling factor, which is related to the chosen defocus. Since, in a Ronchigram, the defocus is very much smaller than the focal length, it is usually well justified to ignore the post-sample effects.

However, if we use the (inverse) magnification to give a measurement of the aberrations, then this assumption will give an error:

$$\boldsymbol{C}_\mathrm{measured} \approx \boldsymbol{C}_\mathrm{true} - \frac{C_{10}}{f}\boldsymbol{D}. \tag{17}$$

In other words, if we use the magnification in the Ronchigram to measure aberrations then, to this level of approximation, we find that each term in the measured aberration function will have an error proportional to the ratio of defocus to the focal length. Again, because the focal length is typically about a thousand times larger than the defocus for a Ronchigram, this error is usually small. However, in a modern aberration corrected system, where the spherical aberration is reduced by a similar factor, this effect might be significant.

4. Experimental demonstration

As a first illustration, we utilize the built-in Nion tuning software and measure the apparent aberrations over ±5 μm, with smaller steps near zero defocus, as shown in Fig. 2. In alignment with Eq. (17), all aberrations along both corrector axes trend in a linear fashion. Using Eq. (17) with a manufacturer suggested focal length of 1.3 mm, we can calculate the true condenser aberrations via the y-intercept and the projector aberrations via the normalized slope.

The measured pre- and post-sample aberrations in Table 1 are reasonable values for a system with a pre-sample (probe) corrector and without a post-sample (image) corrector. For these measurements, not accounting for the post-sample aberrations would lead to almost 60% error in the measurement of $C_{2,1}$.a, which is non-negligible and will lead to incorrect correction of probe aberrations if left unaccounted for.

An alternate method for measuring the aberrations is to create virtual BF images from a 4D-STEM scan using small patches within the BF disc. The virtual BF images from the different patches will be shifted with respect to one another. This method was developed by Lupini co-workers to measure aberrations.[16] It can be thought of as the STEM equivalent of the tilt-induced shift method in TEM,[25] while noting that the application to STEM was again inspired by the pioneering work of Nellist and Pennycook.[1] Notably, this technique can be "used to generate an image with spatial sampling finer than the probe spacing",[17] which has been refined by Ophus[26,27] as "parallax" imaging down to near atomic-scale, and by Kourkoutis and co-workers as "tilt-corrected BF" imaging.[28,29] The method works well for small defocus, which tests Eq. (17) in the low defocus limit. Figures 3(a)–3(e) show a BF focal series acquired from gold nanoparticles on lacy carbon, acquired post-spectrometer using a Dectris ELA, after reconstruction using the parallax method.[26,27] The initial scan parameters were for 256 × 256 probe positions with 0.1 nm step size (giving 25.6 × 25.6 nm field-of-view) and an upsampling of factor of two was used for the BF shifts, which resulted in resolution and signal improvements, as seen by information extending to the Fourier transform limits in Figs. 3(f)–3(j). We also see a clear change in the Thon rings through defocus, some of which are not anti-symmetric about zero defocus, consistent with the presence of post-specimen aberrations.

Table 1. Measured condenser and projector aberrations.

	C_True (nm)		D/f (a.u.)		D (μm)	
	a	b	a	b	a	b
C_{12}	−14.479	8.180	−0.013	0.019	−17.766	25.280
C_{21}	605.459	346.831	0.174	0.049	231.343	64.870
C_{23}	40.990	60.059	−0.026	0.018	−34.891	24.459
C_{30}	13996.553		−0.809		−1075.324	
C_{32}	15567.133	4027.985	1.155	−0.587	1535.724	−780.728
C_{34}	1049.572	328.280	0.023	0.109	30.382	144.654

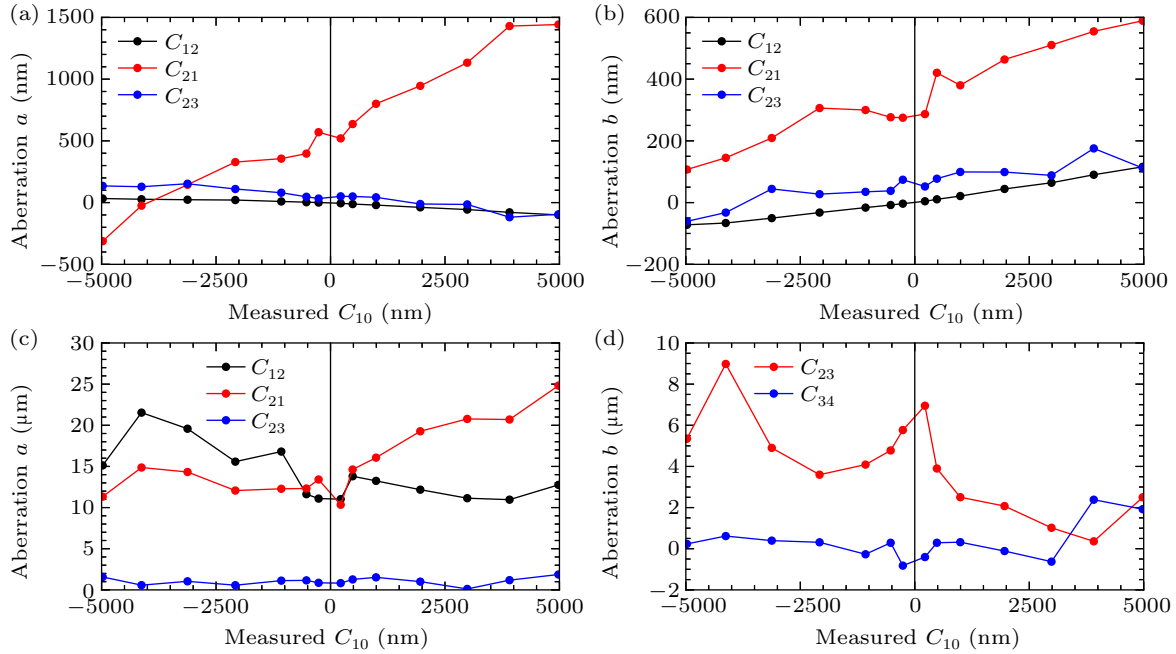


Fig. 2. Measured condenser aberrations for a defocus series spanning ±5 μm using the Nion tuning software. [(a) and (b)] First-, second- and [(c) and (d)] third-order aberrations plotted as a function of measured defocus for the [(a) and (c)] a- and [(b) and (d)] b-axis of the corrector. All show nearly linear trends with non-zero slopes, except for divergences at small defocus.

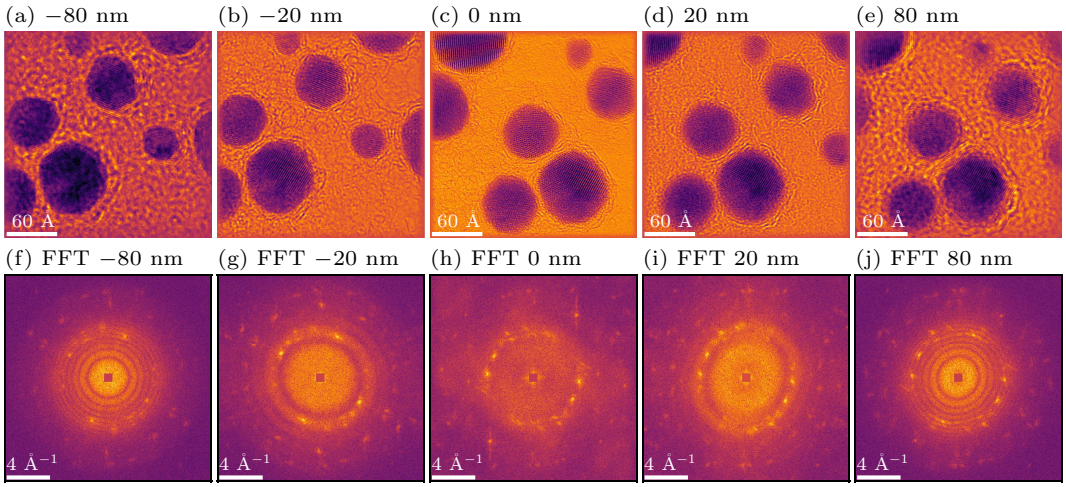


Fig. 3. The 4D-STEM (a)–(e) BF reconstruction using the "parallax" method for nominal defocus spanning ±80 nm and their (f)–(j) Fourier transform.

Figure 4(a) shows the BF shifts measured from the focal series in Figs. 3(a)–3(e). It is important to note that the post-spectrometer detection could dramatically worsen or improve post-specimen geometric aberrations relative to the projectors, or also alter chromatic aberrations. We see from Figs. 4(b) and 4(c) that substantial post-specimen coma exists (C_{21}), which is consistent with the focal series in Figs. 2(a) and 2(b). We note that the axes are not at the same orientation as the corrector, so a- and b-axis values are not directly comparable. The apparent inflection in the C_{21} b-axis is a result of one measurement (the highest defocus at 80 nm), which might be attributed to an incorrect measurement of higher-order aberrations (e.g., it has a high C_{30}) and the fact that aberration measurements are dependent on the reliability of other measured aberrations. Nonetheless, the measurement of post-specimen coma demonstrates that measurement of BF shifts in a defocus series can discriminate between pre- and post-sample aberrations.

The consistent measurement of post-specimen aberrations using both methods has implications for the accuracy of what is typically defined as the probe function. To reiterate a previous statement, the probe function that includes pre-sample aberrations is defined over the image forming aperture, while the post-sample aberrations are distributed continuously as a function of angle in the detected signal. The measured aberrations from 4D-STEM methods will be the combination of complex series of pre- and post-sample aberrations convolved in different planes of the microscope. In other words, the measured probe function is really an instrument function. We have found that to measure condenser

aberrations for a probe-corrector with improved accuracy the post-specimen aberrations should be considered. Similarly, a discrimination between pre- and post-specimen aberrations in a ptychographic instrumental function could allow for better and more realistic constraints during more sophisticated reconstruction.

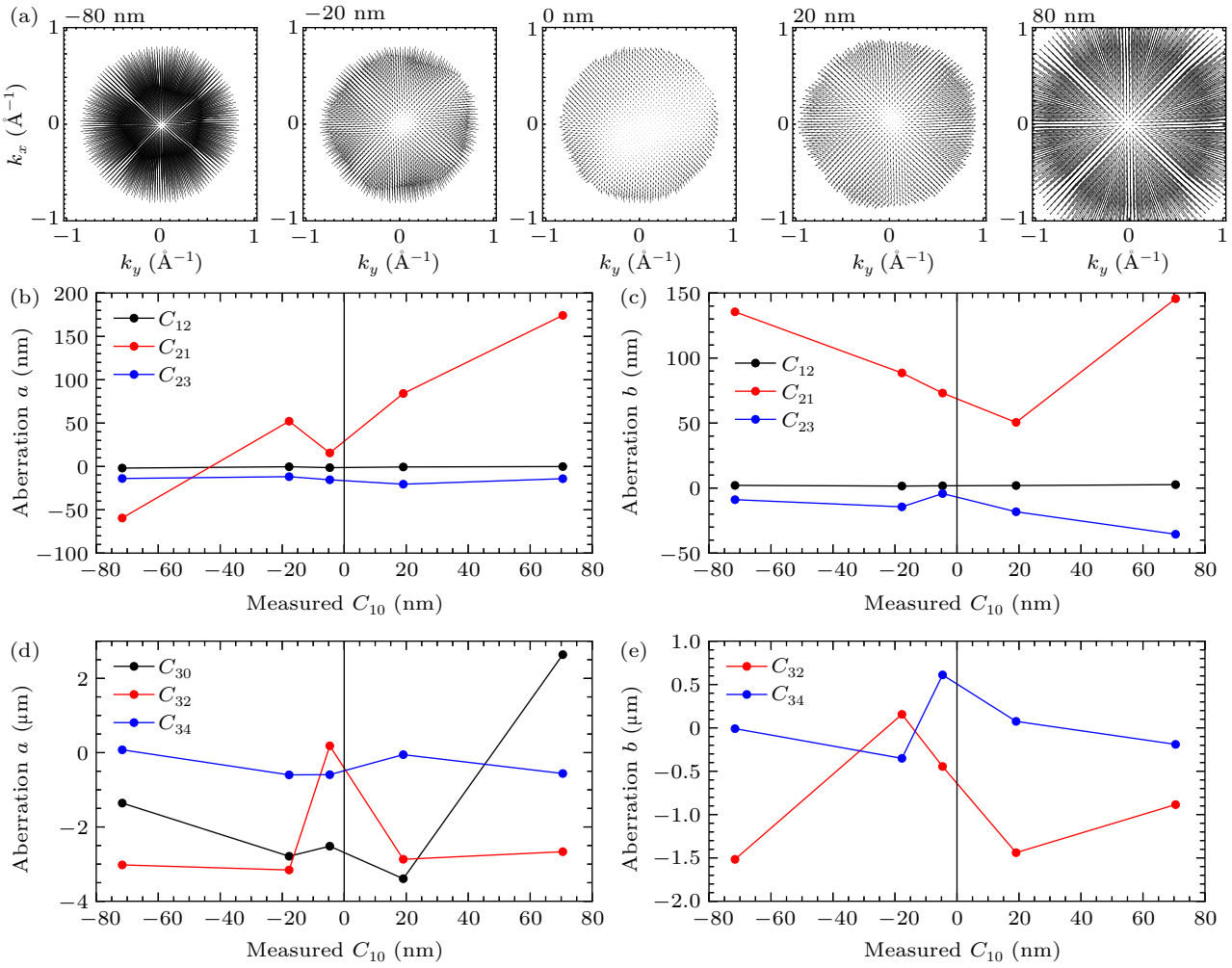


Fig. 4. (a) Vector field of the BF image shifts induced by pre- and post-sample aberrations as a function of nominal defocus spanning ±80 nm showing larger shifts for larger absolute defocuses. [(b) and (c)] First-, second- and [(d) and (e)] third-order aberrations plotted as a function of measured defocus for the [(b) and (d)] a- and [(c) and (e)] b-axis of the corrector.

5. Conclusion

We have shown that post-sample aberrations change the numerical values of the aberrations that are measured when looking at the electron Ronchigram. One method of discriminating between the pre- and post-sample aberrations is an aberration measurement as a function of defocus, which we demonstrate using built-in tuning software and measured virtual BF shifts in 4D-STEM scans. The effect of post-sample aberrations might be apparent when looking at off-axial detectors or using beam tilt. Notably pre-sample aberration might also produce a similar effect in TEM due to the principle of reciprocity.

In many cases, the effect of post-sample aberrations should be small enough to neglect. However, for the case of a single aberration-corrected STEM, when trying to eliminate all residual pre-sample aberrations, this effect should be considered to improve the accuracy of the measurement. This effect probably should not be relevant for annular dark field only methods but will affect STEM phase contrast techniques. It might also be interesting to measure the magnitude of this effect in a double-corrected instrument.

This result should be relevant for ptychography. A simplified view of ptychography is that it uses a series of overlapping Ronchigrams to recover an object function and probe function. Since the recovered probe depends on the apparent aberrations, the recovered probe might be different from the true probe and instead represent an instrument function. This error depends on the defocus condition, so a potential solution is to work at a small defocus where this error can be neglected. Alternatively, separation of the two aberration functions may allow for more physical constraints during reconstruction. A possibly superior solution would be to use 4D-STEM data recorded at different focus values, allowing the pre- and post-sample aberrations to be disentangled, which might naturally

be called 5D-STEM.

Acknowledgments

E.R.H. and A.R.L. acknowledge supported by the U.S. Department of Energy, Office of Basic Energy Sciences (DOE-BES), Division of Materials Sciences and Engineering under contract ERKCS89. We acknowledge support for 4D-STEM performed as part of user proposal at the Center for Nanophase Materials Sciences (CNMS), which is a US Department of Energy, Office of Science, User Facility. Microscopy performed using instrumentation within ORNL's Materials Characterization Core provided by UT-Battelle, LLC, under Contract No. DE-AC05-00OR22725 with the DOE and sponsored by the Laboratory Directed Research and Development Program of Oak Ridge National Laboratory, managed by UT-Battelle, LLC, for the U.S. Department of Energy.

This manuscript has been authored by UT-Batelle, LLC, under Contract No. DE-AC05000R22725 with the U.S. Department of Energy. The United States Government retains and the publisher, by accepting the article for publication, acknowledges that the United States Government retains a non-exclusive, paid-up, irrevocable, world-wide license to publish or reproduce the published form of this manuscript, or allow others to do so, for the United States Government purposes. The Department of Energy will provide public access to these results of federally sponsored research in accordance with the DOE Public Access Plan (http://energy.gov/downloads/doe-public-access-plan).

References

[1] Nellist P D and Pennycook S J 1998 *Journal of Microscopy* **190** 159
[2] Nellist P D and Pennycook S J 1998 *Phys. Rev. Lett.* **81** 4156
[3] Nellist P D, Chisholm M F, Dellby N, Krivanek O L, Murfitt M F, Szilagyi Z S, Lupini A R, Borisevich A, Sides W H and Pennycook S J 2004 *Science* **305** 1741
[4] Rodenburg J M, McCallum B C and Nellist P D 1993 *Ultramicroscopy* **48** 304
[5] Ronchi V 1964 *Appl. Opt.* **3** 437
[6] Hoppe W 1982 *Ultramicroscopy* **10** 187
[7] Rodenburg J M 2008 *Advances in Imaging and Electron Physics* (Elsevier) pp. 87–18
[8] Lin J A and Cowley J M 1986 *Ultramicroscopy* **19** 31
[9] Wang S and Cowley J M 1995 *Microscopy Res. & Technique* **30** 181
[10] Cowley J M 1979 *Ultramicroscopy* **4** 413
[11] Krivanek O L, Dellby N and Lupini A R 1999 *Ultramicroscopy* **78** 1
[12] Sawada H, Sannomiya T, Hosokawa F, Nakamichi T, Kaneyama T, Tomita T, Kondo Y, Tanaka T, Oshima Y, Tanishiro Y and Takayanagi K 2008 *Ultramicroscopy* **108** 1467
[13] Boothroyd C B 1997 *Scanning Microscopy International* **11** 31
[14] Lupini A R and Pennycook S J 2008 *Microscopy* **57** 195
[15] Ramasse Q M and Bleloch A L 2005 *Ultramicroscopy* **106** 37
[16] Lupini A R, Chi M and Jesse S 2016 *Journal of Microscopy* **263** 43
[17] Lupini A R, Chi M, Kalinin S V, Borisevich A Y, Idrobo J C and Jesse S 2016 *Microsc. Microanal.* **22** 252
[18] Pennycook T J, Lupini A R, Yang H, Murfitt M F, Jones L and Nellist P D 2015 *Ultramicroscopy* **151** 160
[19] Yang H, Pennycook T J and Nellist P D 2015 *Ultramicroscopy* **151** 232
[20] Zemlin F, Weiss K, Schiske P, Kunath W and Herrmann K H 1978 *Ultramicroscopy* **3** 49
[21] Krivanek O L and Mooney P E 1993 *Ultramicroscopy* **49** 95
[22] Spence J C H 2013 *High-Resolution Electron Microscopy* (Oxford University Press) pp. 289–314
[23] Lupini A R 2011 *Scanning Transmission Electron Microscopy* (Pennycook S J and P Nellist D, Eds.) (New York: Springer New York) pp. 117–161
[24] Lupini A R, Wang P, Nellist P D, Kirkland A I and Pennycook S J 2010 *Ultramicroscopy* **110** 891
[25] de Jong A F, Koster A J, Video T, de Jong **n.d.**
[26] Terzoudis-Lumsden E W C, Petersen T C, Brown H G, Pelz P M, Ophus C and Findlay S D 2023 *Microscopy and Microanalysis* **29** 1409
[27] Terzoudis-Lumsden E, Petersen T, Brown H, Pelz P, Ophus C and Findlay S 2022 *Microscopy and Microanalysis* **28** 404
[28] Nguyen K X, Purohit P, Hovden R, Turgut E, Tate M W, Kourkoutis L F, Fuchs G D, Gruner S M and Muller D A 2016 *Microsc. Microanal.* **22** 1718
[29] Yu Y, Spoth K A, Colletta M, Nguyen K X, Zeltmann S E, Zhang X S, Paraan M, Kopylov M, Dubbeldam C, Serwas D, Siems H, Muller D A and Kourkoutis L F 2024 *bioRxiv*